Effect of coherent edge mode on high−performance transition in KSTAR hybrid scenario discharges

KSTAR 하이브리드 시나리오 방전의 고성능 천이에 대한 가장자리 코히어런트 모드의 영향 연구

2022 년 8 월

서울대학교 대학원

에너지시스템공학부

이 영 호

Effect of coherent edge mode on high-performance transition in KSTAR hybrid scenario discharges

지도 교수 나 용 수

이 논문을 공학박사 학위논문으로 제출함
2022 년 8 월

서울대학교 대학원
에너지시스템공학부 원자핵공학 전공
이 영 호

이영호의 공학박사 학위논문을 인준함
2022 년 6 월

위 원 장 　　　함 택 수　　　　　(인)

부위원장 　　　나 용 수　　　　　(인)

위　　원 　　　황 용 석　　　　　(인)

위　　원 　　　윤 시 우　　　　　(인)

위　　원 　　　성 충 기　　　　　(인)

Abstract

For the successful operation of a fusion reactor in the future, high performance with a long duration is essential. However, fusion plasmas are complex systems and evolve self−consistently, so understanding the mechanism of high−performance transition and sustainment is challenging. In Korea Superconducting Tokamak Advanced Research (KSTAR), the high performance in hybrid scenarios, one of the candidate operation scenarios in International Thermonuclear Experimental Reactor (ITER), has been investigated for years. In this dissertation, coherent edge mode (CEM) is suggested to play a role in the high−performance transition and sustainment in the KSTAR hybrid scenarios.

CEM is a coherent electromagnetic mode and is localized in the edge region. In the edge localized mode (ELM) crash cycles, CEM is triggered in the middle of the pedestal recovery phase and stabilized after the following ELM crash. CEM tends to increase particle and heat transport in the edge region, resulting in a wide pedestal and decreased plasma density. Interestingly, those two results induced by the increased edge transport contribute to the edge and core confinement improvement, respectively.

With a wide pedestal, ELM crash becomes delayed and weakened. Because of the extended pedestal recovery phase, the pedestal height is further increased. In addition, the enhanced pedestal is not completely lost due to the weakened ELM crash, so the thermal energy confined in the edge region is permanently improved.

The decrease of plasma density, the other result, contributes directly to the fast ion confinement and indirectly to the core thermal confinement. At the reduced plasma density, thermalization of fast ions is delayed, which means fast ions injected externally stay longer in the core plasma. In other words, the number of confined fast ions is increased, resulting in the total fast ion energy improvement. Meanwhile, core thermal energy is enhanced by the stabilization of ion temperature gradient (ITG) mode, the primary microturbulence

limiting the core thermal confinement. Two dominant stabilization effects are revealed by the linear analysis of the microturbulence utilizing the gyrokinetic code, GKW; One is the electromagnetic effect and the other is the ion and electron temperature ratio. The former could be enhanced due to the increased fast ion confinement, and the latter due to the reduced collisionality.

Table of Contents

Chapter 1. Introduction

1.1. Background

Fusion energy is one of the promising concepts of power generation in the future, which utilizes energy emitted by fusion reactions between relatively light ions such as hydrogen isotopes. For the successful operation of a fusion reactor, high performance with a long duration is essential. In the well－known magnetically confined fusion plasma concept, the high performance with a long duration indicates sustaining significant energy contained in a fusion plasma for a considerable period. However, since fusion plasmas are complicated in that electromagnetic fluid evolves self－consistently, understanding the mechanism of the high－performance transition and sustainment is challenging. Hence, advanced operation scenarios for high performance with a long duration have been investigated in many present－day fusion experimental devices for decades.
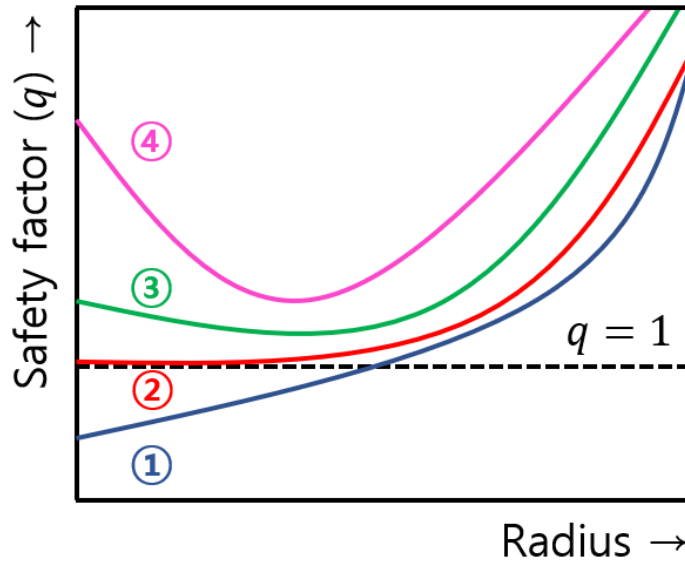

Figure 1.1. Various safety factor, q, profiles. ① is monotonic q, ② flat q or low magnetic shear, ③ weakly reversed magnetic shear,

and ④ strongly reversed magnetic shear.

Hybrid scenarios are one of the advanced operation scenarios and characterize low magnetic shear with a safety factor above or near unity in the core region [1-3], as ② in figure 1.1. Due to this characteristic safety factor profile, hybrid scenarios have better stability and confinement. For example, well−known sawtooth instabilities, a trigger for the devastating neoclassical tearing mode (NTM), are stabilized [4], so operations at higher normalized pressure are available [1]. In addition, the low magnetic shear is known to enhance the electromagnetic stabilization effect [5] on ion temperature gradient (ITG) mode [6], the primary microturbulence limiting the core thermal confinement.
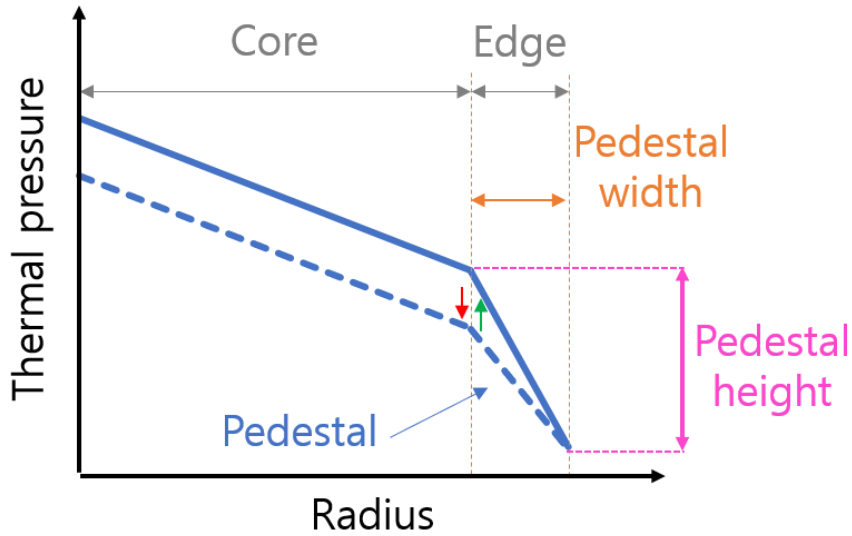

Figure 1.2. Example of thermal pressure profile in H−mode plasma [7]. The pedestal is a structure with a steep thermal pressure gradient in the edge region. The width and height of the pedestal are represented as arrow in orange and magenta, respectively. The red and green arrows indicate the collapse and recovery of the pedestal during edge localized mode, ELM, cycles [8,9].

In the International Thermonuclear Experimental Reactor (ITER) project [10], hybrid scenarios are one of the candidate scenarios. Between the baseline scenarios operated at $15\,MA$ to verify $Q = 10$

for over $300\,s$ and the steady−state scenarios at $9\,MA$ for $Q = 5$ over $3000\,s$, hybrid scenarios are operated at $12\,MA$ for the 'hybrid' goals such as $Q > 5$ for over $1000\,s$. Here, Q is a fusion gain factor defined as the output to input power ratio. Moreover, provided by the improved stability and confinement, hybrid scenarios are prescribed as the advanced tokamak operations in ITER, such as $Q > 10$ operations at $12\,MA$ or $Q > 20$ operations at $15\,MA$. It is noted that all candidate scenarios are based on H−mode operations [7], characterizing the steep gradient region in the edge thermal pressure, called pedestal, as shown in figure 1.2.

1.2. Motivation

The origin of the improved energy confinement in hybrid scenarios has been investigated in present−day fusion experimental devices, and two primary mechanisms have been proposed. One is the core thermal confinement improvement attributed to the ITG mode stabilization provided by magnetic shear [11], $E \times B$ flow shear [12], and electromagnetic effect provided by fast ion pressure and Shafranov shift [5,13]. The other is the edge thermal energy enhancement due to the improved ideal peeling−ballooning mode (PBM) stability in the pedestal resulting from poloidal beta and triangularity [14], where the poloidal beta is defined as the ratio of plasma pressure to poloidal magnetic field pressure.

In Korea Superconducting Tokamak Advanced Research (KSTAR), the fusion experiment device in Korea, the performance improvement process observed in hybrid scenario discharges has been studied for years. In 2020, the performance enhancement process after applying additional external heating was reported [15]. It proposed core−edge coupled performance improvement; First, the core thermal pressure is increased due to the additional core heating, which increases poloidal beta and Shafranov shift. Then, the ideal PBM stability in the pedestal is improved by the enhancement of poloidal beta and Shafranov shift, so a higher pedestal pressure is obtained. Finally, the increase of the pedestal heaves the core

thermal pressure, and the positive feedback of core-edge coupled performance improvement is established.

Even though it provided a reasonable explanation for the process of performance improvement observed after the additional external heating is applied in KSTAR hybrid scenario discharges, it did not cover the case where plasma performance is not improved even after the extra external heating. In fact, in the hybrid scenario experiments in the 2019-2021 KSTAR campaigns, the high-performance criteria, $\beta_N > 2.4$ and $H_{89} \geq 2.0$, defined in [15] were hardly satisfied despite more externally applied heating power than before. Here, β_N is normalized plasma pressure, and H_{89} is the energy confinement time relative to the L-mode global energy confinement scaling [16]. In addition, as will be shown in section 2.1, it has been observed in some hybrid scenario experiments that two discharges operated by the same target scenario have quite different plasma performances. It implies that another physical mechanism is necessary for the high-performance hybrid scenarios in KSTAR.

1.3. Outline of this dissertation

This dissertation suggests that coherent edge mode (CEM) is responsible for the high-performance transition and sustainment in KSTAR hybrid scenario discharges. CEM is a coherent electromagnetic mode and is localized in the edge region. In the edge localized mode (ELM) crash cycles [8,9], the repetitive pedestal collapse and recovery in the H-mode plasmas as described in figure 1.2, CEM is triggered in the middle of the pedestal recovery phase and stabilized after the following ELM crash. During CEM activities, particle and heat transport tends to increase in the edge region, and, consequently, the pedestal becomes broadened, and plasma density is decreased.

Interestingly, those two changes induced by the increased edge transport contribute to the edge and core confinement improvement, respectively. With a wide pedestal, the ELM crash becomes delayed and weakened. Due to the extended pedestal recovery phase, the

pedestal height is further increased. Moreover, the resulting thermal energy in the pedestal is not entirely lost, attributing to the weakened ELM crash. In other words, the thermal energy confined in the pedestal is permanently enhanced.

The decrease of plasma density, the other result of the increased edge transport with CEM activities, contributes directly to the fast ion confinement and indirectly to the core thermal confinement. For the fast ion confinement, thermalization of fast ions is delayed due to the reduced plasma density. It means fast ions stay longer in the core plasma, so the total energy of fast ions becomes enhanced. Meanwhile, the improved fast ion confinement contributes to the core thermal confinement by the ITG mode stabilization provided by the enhanced equilibrium pressure gradient in the core [5,13]. In addition, density decrease is known to enhance the ion and electron temperature ratio by reducing collisional equilibration between ion and electron thermal energy in the case of dominant ion heating [3,17-19], which provides another ITG mode stabilization. The linear analysis of the microturbulence using the gyrokinetic code, GKW [20], shows consistent results; The core thermal confinement improvement is found to be accompanied by the ITG stabilization enhanced predominantly due to the increased equilibrium pressure gradient and the ion and electron temperature ratio.

Section 2 introduces two discharges operated by the same target scenario; One with CEM activities has a high stationary performance of $\beta_N = 2.8$, and the other has $\beta_N = 2.2$. Three phases of different plasma performances are selected in them, and the origin of the high performance is analyzed. In section 3, characteristics of CEM are introduced, and the changes in the plasma under CEM activities is investigated. The effect of CEM on the edge and core confinement is discussed in sections 4 and 5, respectively. Finally, in section 6, all contents are summarized, and future works are listed.

Chapter 2. Performance improvement in

KSTAR hybrid scenario discharges

2.1. Characteristics of the high and low-performance discharges

Several sets of hybrid scenario experiments in KSTAR show that two discharges operated by the same target scenario, such as plasma current, externally applied heating, and boundary shape, have different plasma performances. Figure 2.1 shows a representative case. Both 25452 and 25458 are operated by the same target scenario, but β_N and neutron rate, indicators of plasma performance, are pretty different in the stationary phase; 25452 has $\beta_N = 2.8$ while 25458 has $\beta_N = 2.2$. The neutron rate in 25452 is almost double in 25458.
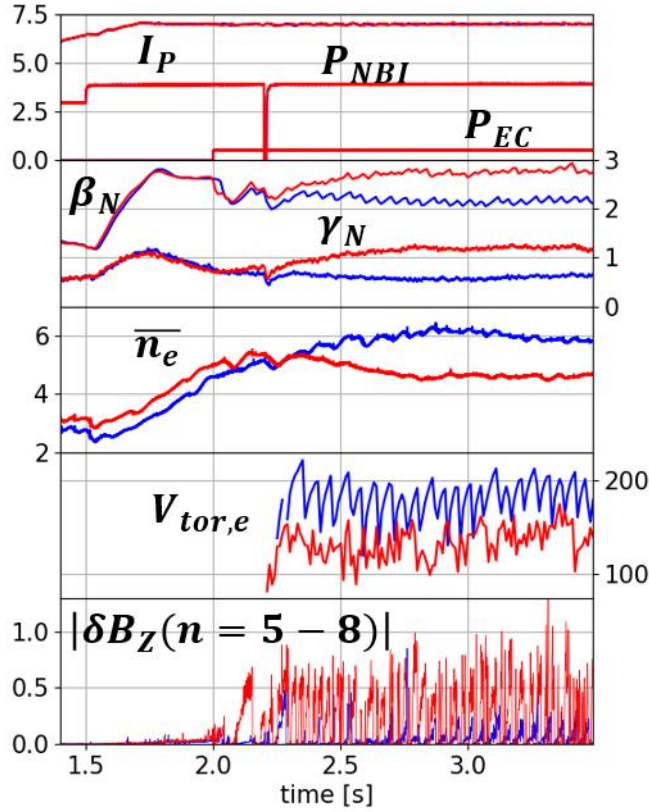
Figure 2.1. Scenario overview for 25452 (red) and 25458 (blue).
I_P, P_{NBI}, and P_{EC} are plasma current in $10^2\ kA$, neutral beam heating power, and electron cyclotron heating power in MW, respectively.
β_N and γ_N are normalized pressure gradient and neutron rate in an arbitrary unit, respectively. $\overline{n_e}$ is line averaged density in $10^{19}\ m^{-3}$.
$V_{tor,e}$ is edge toroidal rotation in km/s. $|\delta B_Z(n = 5{\sim}8)|$ is the summed amplitude of magnetic perturbation of $n = 5-8$ measured by Mirnov coils, where n is the toroidal mode number.

In addition, plasma characteristics, such as a line averaged density, $\overline{n_e}$, and edge toroidal rotation, $V_{tor,e}$, also change in the stationary phase. Compared to 25458, the low−performance discharge, 25452, the high−performance discharge, has lower $\overline{n_e}$, in the stationary phase. The interesting point is that $\overline{n_e}$ in 25452, which is larger than 25458 in the early phase of discharge, decreases during the increase of β_N and neutron rate. It implies the increased particle

7

transport in the high-performance phase and the possible correlation between plasma density and plasma performance. Note that since no external gas fueling is applied in both cases, the slight difference in $\overline{n_e}$ in the early phase of discharge is presumably due to the wall retention, which is not controllable in KSTAR.

On the other hand, the reduced $V_{tor,e}$ is attributable to both increased toroidal momentum transport or decreased momentum source. Even though the externally applied toroidal momentum source, provided predominantly by three neutral beam injections (NBIs), is expected to be the same in 25452 and 25458, residual stress in the pedestal, the other primary toroidal momentum source in KSTAR [21], could vary. Since residual stress is proportional to the fluctuation intensity and $E \times B$ shear, a decrease in the pedestal pressure gradient reduces residual stress and, as a result, $V_{tor,e}$.

Another notable difference between 25452 and 25458 is magnetohydrodynamics (MHD) mode activities. In 25452, a strong MHD mode of toroidal mode number of 5-8 is observed in every inter-ELM crash period. Looking closely, β_N and the neutron rate of 25452 and 25458 begin to diverge near $2.1\,s$, the first emergence of the MHD mode in 25452. It implies that the MHD mode could be related to the high-performance transition.

2.2. Origin of performance improvement

Three phases with different performances are selected for the comparative analysis of performance improvement. From here, 'Low' indicates $2.4\,s$ in 25458, the low-performance phase, and 'High: early' and 'High: stationary' means $2.4\,s$ and $4.05\,s$ in 25452, representing the early and stationary phases of the high performance, respectively. The phase transition from 'Low' to 'High: early' to 'High: stationary' is assumed to analyze the performance improvement process.
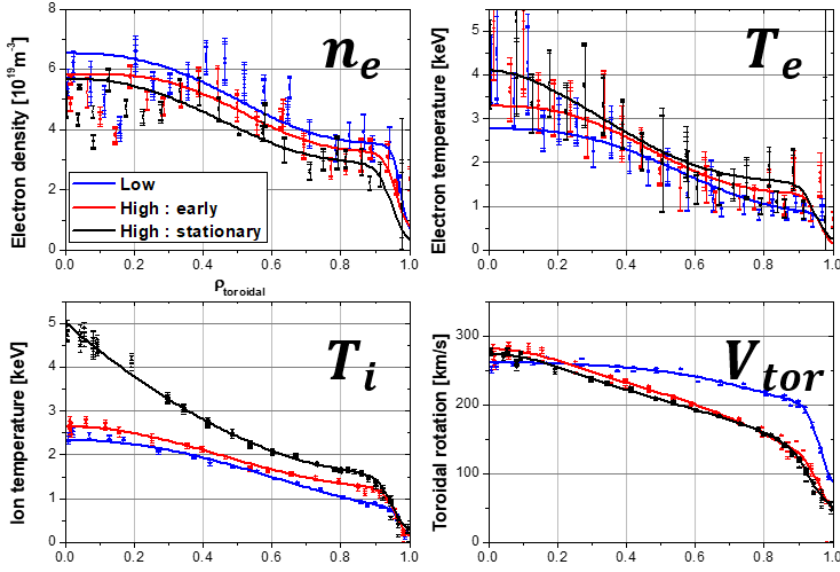
Figure 2.2. Electron density (n_e), electron temperature (T_e), ion temperature (T_i), and toroidal rotation (V_{tor}) profiles for three phases, 2.4 s in 25458 ("Low" in blue), 2.4 s in 25452 ("High:early" in red) and 4.05 s in 25452 ("High:stationary" in black). Note that n_e, T_e and T_i profiles are fitted with an analytic function characterizing hyperbolic tangent shape for pedestal structure [22].

Figure 2.2 shows measured kinetic profiles for each phase. Electron density, n_e, and electron temperature, T_e, were measured by Thomson scattering diagnostics [23], and ion temperature, T_i, and toroidal rotation, V_{tor}, were measured by charge exchange spectroscopy (CES) [24]. Because the temporal and spatial resolution of Thomson scattering diagnostics is too low to follow the pedestal evolution, the repetitive collapse and recovery of the pedestal in ELM cycles, the pedestal width of n_e and T_e was assumed to be the same as that of T_i. In addition, $\overline{n_e}$ measured by five two-color interferometers (TCI) [25] with different line integration paths was constrained in n_e profile fitting to compensate for the measurement errors. $T_e = T_i$ was also assumed for the pedestal region due to considerable uncertainty in the edge T_e. Note that the equilibria to fit the profiles in the normalized toroidal

9

magnetic flux coordinates, $\rho_{toroidal}$, were calculated by EFIT code with kinetic profile constraints [26]. Due to the lack of Motional Stark effect diagnostics (MSE), modeled magnetic pitch angle profiles provided by CHEASE [27], the equilibrium solver, were utilized as an input of the kinetic−EFIT analysis.

The most outstanding point found in the kinetic profiles is the change of pedestal width in each phase. As the performance improves, the pedestal width is getting broadened. In addition, compared to in 'Low', the V_{tor} pedestal gradient is considerably reduced in both 'High' phases, as mentioned in section 2.1. Another notable point is a significantly increased core T_i between 'High: early' and 'High: stationary'.
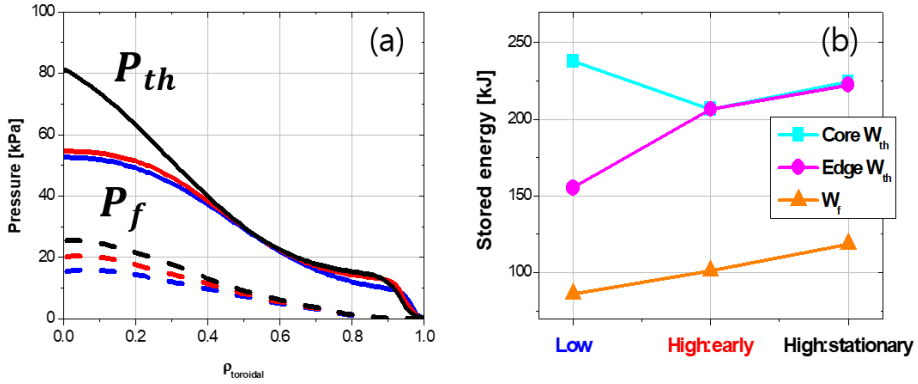

Figure 2.3. (a) Thermal pressure (P_{th}) and fast ion pressure (P_f) profiles. (b) core thermal (Core W_{th}), edge thermal (Edge W_{th}), and fast ion stored energy (W_f) for the three phases described in figure 2.2. P_f and W_f are calculated by NUBEAM code [28].

Figure 2.3(a) shows thermal pressure, P_{th}, and fast ion pressure, P_f. P_{th} is provided by $P_{th} = T_e n_e + T_i n_i$, where n_i is thermal ion density. Note that n_i is determined by quasi−neutrality, assuming fully stripped carbon impurities and an effective ion charge of 1.2 for all radii. P_f is not measurable in KSTAR, so Monte Carlo code NUBEAM [28] was utilized. In the NUBEAM analysis, no anomalous fast ion diffusion was assumed in NUBEAM calculation because there are no MHD modes causing fast ion loss, such as fishbone modes [29]

or Alfven eigenmodes [30], so only neoclassical transport is expected. It is noteworthy that the total stored energy calculated by the volume integration of $3/2\,(P_{th} + P_f)$ in the radial direction is compared to that provided by equilibrium reconstruction code, EFIT, in each phase, and less than 1% difference verifies the assumptions in P_{th} and P_f.

As already introduced in figure 2.2, the increasing pedestal width with performance is also shown in P_{th}. On the other hand, the pedestal height, a dominant parameter determining the edge thermal energy confinement, is increased primarily from 'Low' to 'High: early' and slightly between 'High: early' and 'High: stationary'. Notably, the peak value of the pedestal pressure gradient decreases as the pedestal width increases. Meanwhile, the increase of core P_{th} is only observed for the inner core region of $\rho_{toroidal} < 0.5$ between 'High: early' and 'High: stationary'. The centrally peaked P_f attributed to the on−axis NBI configurations increases as the performance improves.

For the quantitative performance improvement analysis, figure 2.3(b) represents the core and edge thermal energy and the fast ion energy in each phase. For thermal energy, the edge thermal energy is defined as the total thermal energy increased by the pedestal structure, and the rest is the core thermal energy. From 'Low' to 'High: early', the edge thermal energy increases by $51.1\,kJ$ while the core thermal energy decreases by $31.4\,kJ$. The increase in the edge thermal energy is attributable to the increased pedestal height and width. In other words, the pedestal volume is expanded with the height increase. On the other hand, the core thermal energy is decreased due to the reduced core volume resulting from the increased pedestal volume. Additionally, the broken stiffness of P_{th} is found in the outer core region, $\rho_{toroidal} > 0.7$, so the increased pedestal height does not lift the core P_{th}. From 'High: early' to 'High: stationary', the core and edge thermal energy are increased by 17.6 and $15.9\,kJ$, respectively. As before, the edge thermal energy increase results from the enhanced pedestal height and width. However, the increase in the pedestal height is relatively small, as

mentioned above, so the edge thermal energy increase is limited. Notably, the core thermal energy increases in this case despite the core volume decrease. This is because the core thermal confinement improves in the inner core region, $\rho_{toroidal} < 0.5$, enough to compensate for the reduced core volume effect. Meanwhile, fast ion energy increases by **15.2** and **17.3** kJ in each performance improvement. In short, performance improvement originates from the edge thermal and fast ion energy, which are enhanced by **67** kJ and **32.5** kJ, respectively. Even though the net core thermal energy change is negative, the core thermal energy decrease is limited by the confinement improvement in the inner core region between 'High: early' and 'High: stationary'.
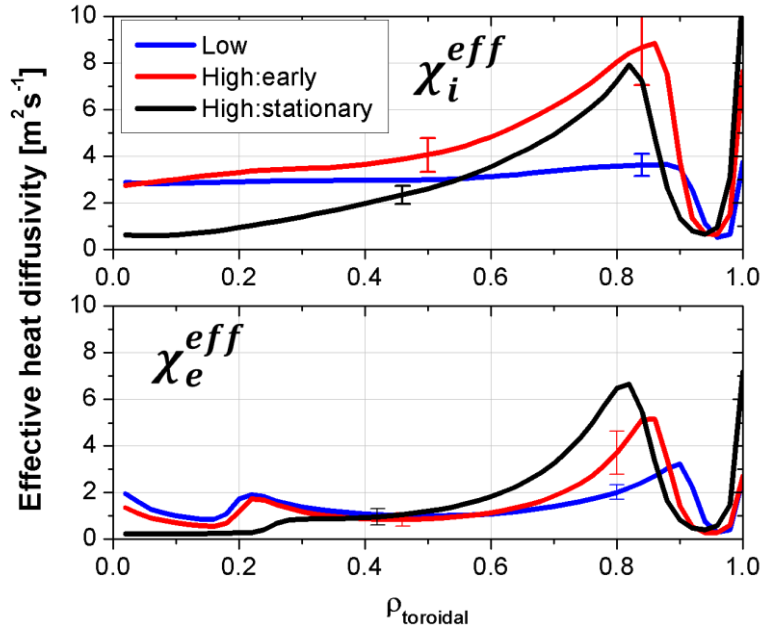

Figure 2.4. Ion (χ_i^{eff}) and electron (χ_e^{eff}) effective heat diffusivity profiles calculated by power balance analysis for the three phases described in figure 2.2. Note that the error bars were determined by considering available fitted profiles within the error bars of each measured profiles.

In figure 2.4, effective heat diffusivity is shown for each phase. Effective heat diffusivity is calculated by power balance analysis. Power balance analysis assumes heat diffusion as the dominant heat

transport mechanism for the state of the equilibration between outgoing and incoming heat flux, i.e., thermal equilibrium. Consequently, the equation, $q_{out} = q_{in} = \chi^{eff} n \nabla T$, is valid, so effective heat diffusivity, χ^{eff}, is obtained by $q_{in}/n\nabla T$. Here, q_{out}, q_{in}, n, and ∇T are outgoing and incoming heat flux, density, and temperature gradient, respectively. From 'Low' to 'High: early', effective ion and electron heat diffusivities, χ_i^{eff} and χ_e^{eff}, increase around $\rho_{toroidal} = 0.8$, where the stiffness of P_{th} is broken. It implies that the decrease in the thermal pressure gradient could be due to the increased ion and electron heat transport for some reason. The enhanced χ_i^{eff} and χ_e^{eff} are sustained for the 'High' phases, which is shown as the reduced ∇P_{th} in the outer core region in both 'High' phases in figure 2.3(a). Comparing 'High: early' and 'High: stationary', the decrease of χ_i^{eff} and χ_e^{eff} in the inner core region is conspicuous. It reveals that the improvement of P_{th} for $\rho_{toroidal} < 0.5$ is attributable to reduced ion and electron heat transport, i.e., improved thermal confinement. Note that the decrease in χ_i^{eff} is more significant than in χ_e^{eff}, which is consistent with figure 2.2, where the core T_i increases more than the core T_e. Meanwhile, the radial extension of the low χ_i^{eff} and χ_e^{eff} region near $\rho_{toroidal} = 0.95$ represents pedestal broadening in each performance improvement.

Chapter 3. Coherent edge mode

As mentioned in section 2.1, the high−performance phase in 25452 is accessed and sustained with strong MHD mode activities. Therefore, it is necessary to analyze the effect of the MHD mode on the high−performance transition and sustainment introduced in section 2.2. Before that, the MHD mode characteristics are shown in this section.

3.1. Characteristics of coherent edge mode

The MHD mode is an electromagnetic mode observable in the magnetic field fluctuation measurement, Mirnov coils. π-phase jump in radius, which is a representative characteristic of the magnetic island structure, is not found, so it is thought to be an ideal mode.
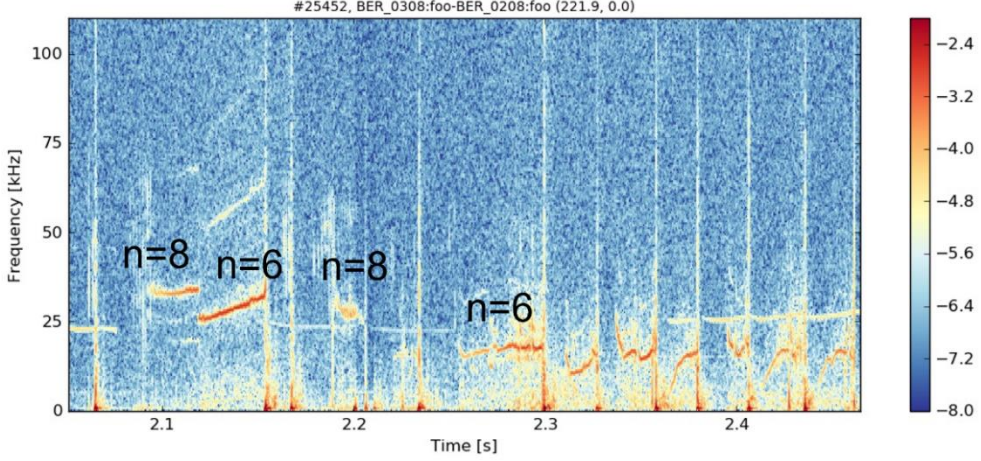

Figure 3.1. Spectrogram of normalized beam emission intensity fluctuation, $(I_{BES} - \langle I_{BES} \rangle)/\langle I_{BES} \rangle$, near the separatrix region in 25452 measured by beam emission spectroscopy. <> means time averaging, and the "n=X" text notifies the toroidal mode number, X, of the coherent mode.

Figure 3.1 shows the spectrogram of the normalized beam emission intensity fluctuation, representing normalized n_e fluctuation, measured by beam emission spectroscopy (BES) [31] near the separatrix in 25452, the high-performance discharge introduced in section 2. The mode is a coherent mode with a single frequency, and the toroidal mode number is 6 or 8 in this case. The mode is triggered in the inter-ELM crash period, specifically in the middle of the pedestal recovery phase, and stabilized after the ELM crash. Sometimes, it is intermittently stabilized and retriggered during one inter-ELM crash period, such as near $2.28\,s$ or $2.34\,s$. After the mode is triggered, it grows slowly or almost saturates in amplitude, which characterizes a long lifetime up to several tens of milliseconds, sometimes accounting for about $90\,\%$ of the whole inter-ELM crash period.
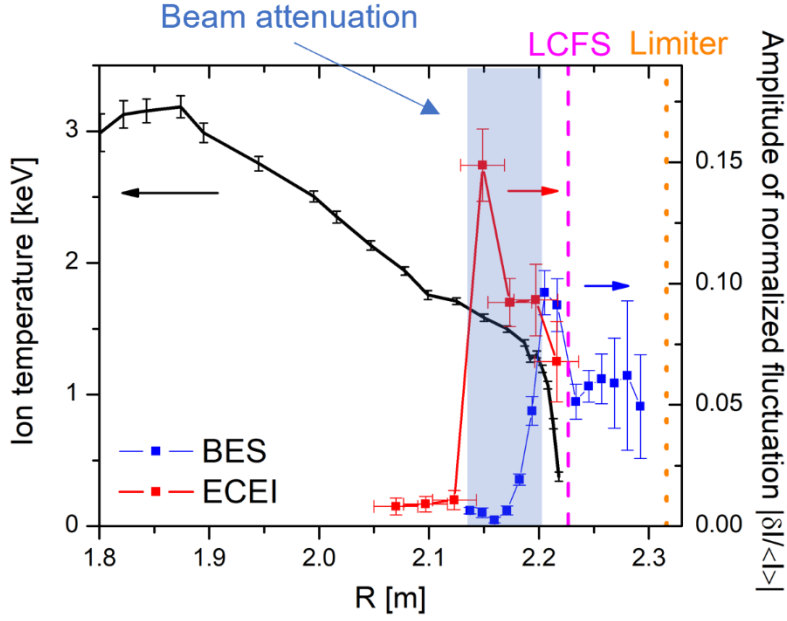
Figure 3.2. The ion temperature and normalized fluctuation amplitude profiles at 2.4 s in 25452. The normalized fluctuation amplitude is measured by BES and electron cyclotron emission imaging (ECEI) and filtered for the frequency of the coherent mode. The magenta dashed and the yellow dotted lines indicate the last closed flux surface (LCFS) and outer limiter location, respectively. The blue shaded region represents the BES channels susceptible to beam attenuation.

In figure 3.2, the normalized fluctuation amplitude measured by BES and electron cyclotron emission imaging (ECEI) for the normalized electron temperature fluctuation [32] is compared with T_i profile. The mode is found to be localized in the edge region, so coined coherent edge mode (CEM). Interestingly, CEM is not only localized in the steep pedestal region but also has finite amplitude in the outer core region, inside the pedestal top, and the scrape−off layer (SOL). In other words, it has a large scale of mode structure, distinguishing it from the mode localized in the steep pedestal region with a fine structure, such as kinetic ballooning mode (KBM) [33].
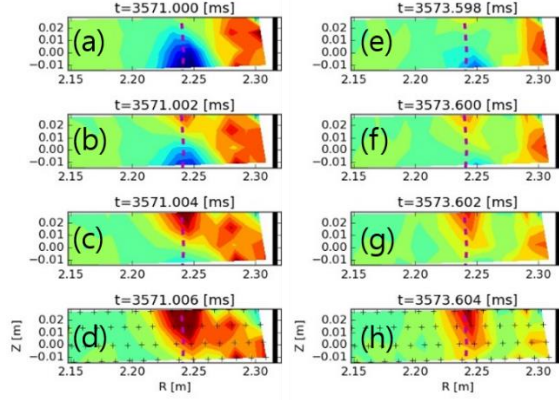
Figure 3.3. Normalized BES intensity fluctuation images when (a−d) CEM amplitude saturates and (e−h) CEM is intermittently stabilized in 26417. The dashed magenta and solid black lines indicate LCFS and outer limiter location, respectively. In (d) and (h), BES channels are represented as small crosses.

CEM is similar to the pre−ELM crash MHD oscillations. Firstly, CEM and the pre−ELM crash MHD oscillations are localized in the edge region [9,34]. Secondly, as shown in figure 3.3(a−d), CEM has a filament structure stretched into the SOL, as the pre−ELM crash MHD oscillations [35-39]. Thirdly, in some cases, both have a phase with saturated mode amplitude [37,40]. Finally, the stabilization of the pre−ELM crash MHD oscillations with falling of filaments [[36-38]] with leaving a H_α line intensity peak, i.e., ELM crash, are also similar to the intermittent stabilization of CEM shown in figure 3.3(e−h) and, as will be shown, in figure 3.4. Nevertheless, CEM is distinguishable from the pre−ELM crash MHD oscillations in that CEM has an order of magnitude longer lifetime and smaller peaks of H_α line intensity. Additionally, the pedestal T_e is hardly changed at the intermittent stabilization of CEM while it is collapsed at the ELM crash, as will be seen in figure 3.4.

It is informed that the different peak locations of the normalized fluctuation of BES and ECEI in figure 3.2 are because of the beam attenuation effect on BES. Since BES measures the light intensity emitted by the interaction between beam ions and background electrons, the phase of the intensity fluctuation of BES could be flipped inside due to destructive interference. For example, if it is the

crest of density fluctuation in the outer region, it attenuates beam
ions more, resulting in decreased BES intensity, the trough, in the
inner. Since the KSTAR hybrid scenario discharges are typically
operated at a relatively high density than other H−mode scenarios,
the beam attenuation effect is expected to be stronger. Therefore,
the peak location of the normalized fluctuation of BES is unknown in
figure 3.2 but probably more inside.

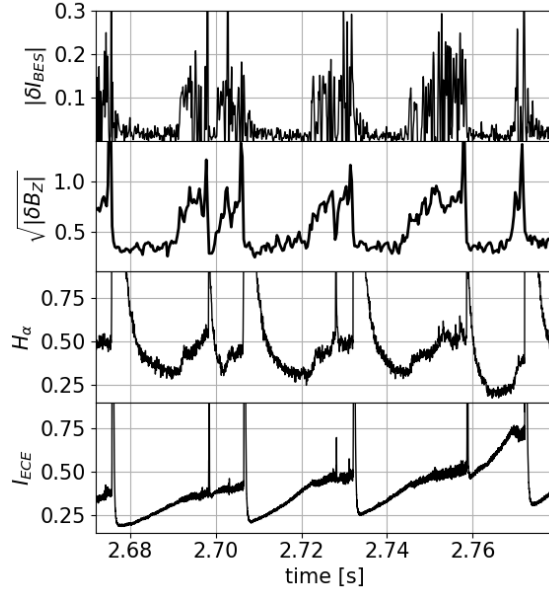## 3.2. Effect of coherent edge mode on plasma

Figure 3.4. CEM fluctuation amplitude measured by BES ($|\delta B_{BES}|$),
CEM mode amplitude by Mirnov coils ($|\delta B_Z|$), H_α line intensity at
the lower divertor region, and electron cyclotron emission intensity
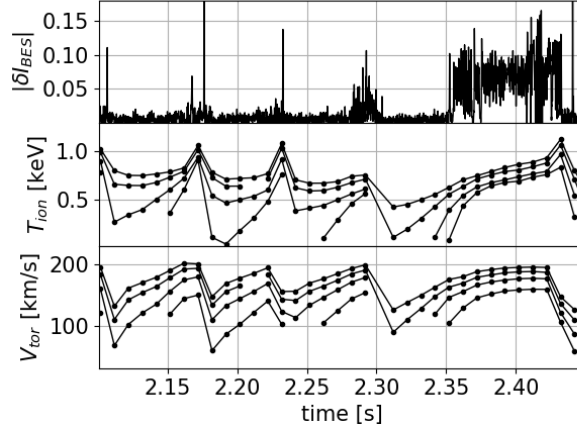near the pedestal top (I_{ECE}) in 25452.

Figure 3.5. CEM fluctuation amplitude measured by BES ($|\delta B_{BES}|$), ion temperature (T_{ion}), and toroidal rotation (V_{tor}) measured by four channels around the edge region in 28030.

CEM activities tend to increase edge transport. Figure 3.4 shows CEM amplitude measured by BES and Mirnov coil, H_α line intensity at the lower divertor region, and electron cyclotron emission intensity, I_{ECE}, near the pedestal top region. It is shown that H_α line intensity increases with CEM amplitude, and the increase of I_{ECE} becomes slow after the CEM onset. Since H_α line intensity is roughly proportional to the number of particles, particle transport is believed to be increased in plasma during CEM activities. Similarly, because I_{ECE} is proportional to the pedestal top electron temperature, the slowing down of I_{ECE} increase after the CEM onset can be interpreted as the increased electron heat transport during CEM activities. The change in H_α intensity and I_{ECE} due to CEM activities is more evident after 2.759 s, the intermittent stabilization of CEM; H_α intensity goes down, and I_{ECE} increase is accelerated. A Similar trend is also found in the edge ion temperature and toroidal rotation. Figure 3.5 shows the edge ion temperature and toroidal rotation evolution during four ELM cycles, where CEM is triggered in the last ELM cycle. Compared to the three ELM cycles without CEM activities before 2.32 s, the decreased recovery rate of the edge ion temperature and toroidal rotation is observed after the CEM onset at 2.35 s. In other words, CEM activities tend to increase the ion heat

and, possibly, toroidal momentum transport in the edge region. Note that the edge toroidal rotation is affected by residual stress as well as toroidal momentum, as discussed in section 2.1. In short, CEM tends to increase particle, heat, and toroidal momentum transport in the edge region.

Considering CEM has a finite amplitude in the outer core region as mentioned in section 3.1, CEM might be responsible for the broken stiffness of P_{th} and the increased ion and electron heat diffusivities in the outer core region between 'Low' and 'High: early' introduced in section 2. It is noted that, as mentioned earlier in section 3.1, intermittent stabilization of CEM at **2.698**, **2.727**, and **2.759** s leaves H_α line intensity peak much smaller than that at the ELM crash, such as **2.732** s.
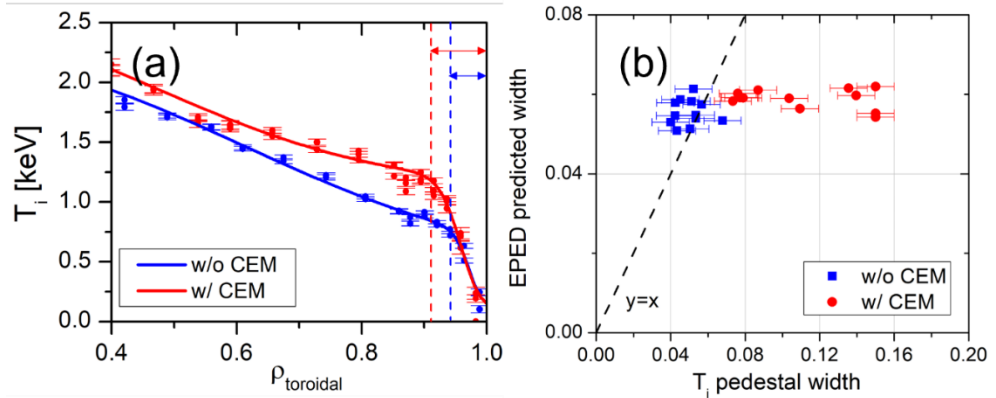

Figure 3.6. Close−up of ion temperature (T_i) profiles of 25458 without CEM ("w/o CEM" in blue) and 25452 with CEM ("w/ CEM" in red). (b) Measured ion temperature (T_i) pedestal width vs. the pedestal width predicted by EPED model for the cases without CEM ("w/o CEM" in blue squares) and with CEM ("w/ CEM" in red circles). 25458 and 28025 are selected for the case without CEM, while 25452 and 28029 are for with CEM.

With CEM, there are two primary changes in plasma related to the increased transport. One is pedestal broadening, and the other is density decrease.

Figure 3.6(a) shows the close−up of the outer ion temperature profiles of 'Low' and 'High: early' shown in figure 2.2, which represents the pedestal structure at the end of the pedestal recovery

1 9

phase without and with CEM activities, respectively. As mentioned in section 2.1, the wider pedestal width is observed in 'High: early', where CEM exists.

For generalization, figure 3.6(b) compares measured and predicted pedestal width evaluated in the normalized poloidal flux coordinates in cases without and with CEM activities. The measured one is from the ion temperature pedestal selected right before the ELM crash, and the predicted one is provided by the well-known EPED model [41]. EPED model assumes that pedestal width and height during the pedestal recovery are determined by the transport characteristics, such as KBM activities, and ELM crash is triggered by the linear stability of ideal PBM. Since the characteristic paths of pedestal width and height are different for KBM and ideal PBM stability, the intersection of the two indicates pedestal width and height at ELM crash.

For inputs to the EPED model, equilibrium was reconstructed by kinetic-EFIT with magnetic pitch angle profile modeled by CHEASE code. The line averaged density measured for the outer region [25] is used to determine the pedestal top density. Separatrix density and temperature are assumed to be $5 \times 10^{18} m^{-3}$ and $0.1\ keV$, respectively.

Without CEM, the measured and predicted width are similar. On the other hand, for the case with CEM, the measured width is larger than the predicted one. Since the pedestal width is related to transport characteristics as introduced above, the measured pedestal width larger than the prediction implies the increased transport in the pedestal. It is consistent with the tendency that the edge transport is increased with CEM activities compared to without CEM activities.
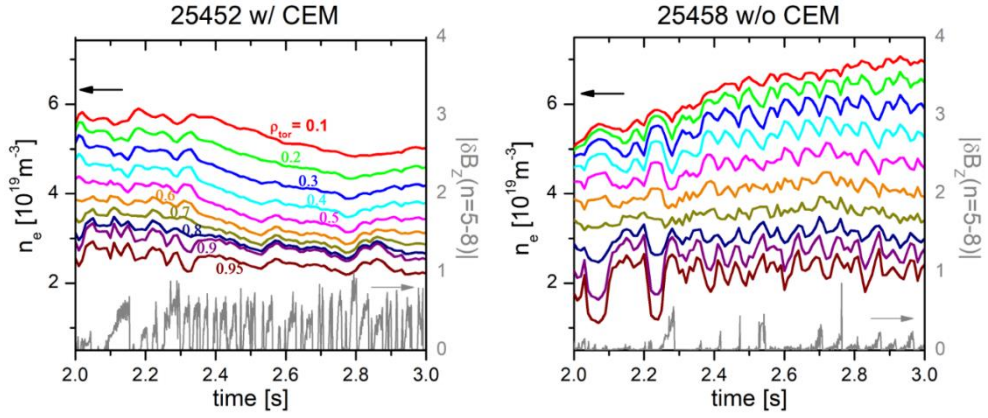
Figure 3.7. Electron density (n_e) evolution at each $\rho_{toroidal}$ and the amplitude of magnetic fluctuation of $n = 5 - 8$ measured by Mirnov coils ($|\delta B_Z(n = 5 - 8)|$). The left is 25452 with CEM, and the right is 25458 without CEM. n_e is reconstructed by five line averaged density measurements with different integration paths and equilibria.

The other primary change observed with CEM activities, density decrease, is represented in figure 3.7. Figure 3.7 compares electron density evolution in 25452 with CEM and 25458 without CEM. Note that the electron density was reconstructed by the five independent line average density measurements with different integration paths and equilibria at each time slice. In 25452, plasma density in all radial locations decreases after the first CEM onset near $2.1\,s$. On the other hand, in 25458, plasma density, smaller than in 25452 at first, continues to increase, and $40\,\%$ larger stationary electron density compared to in 25452 is obtained. Because both discharges were operated by the same target scenario and no external fueling was applied as introduced in section 2.1, the continuous decrease of electron density seems to be related to the increased particle transport during CEM activities.

Chapter 4. Effect of CEM on the edge confinement improvement
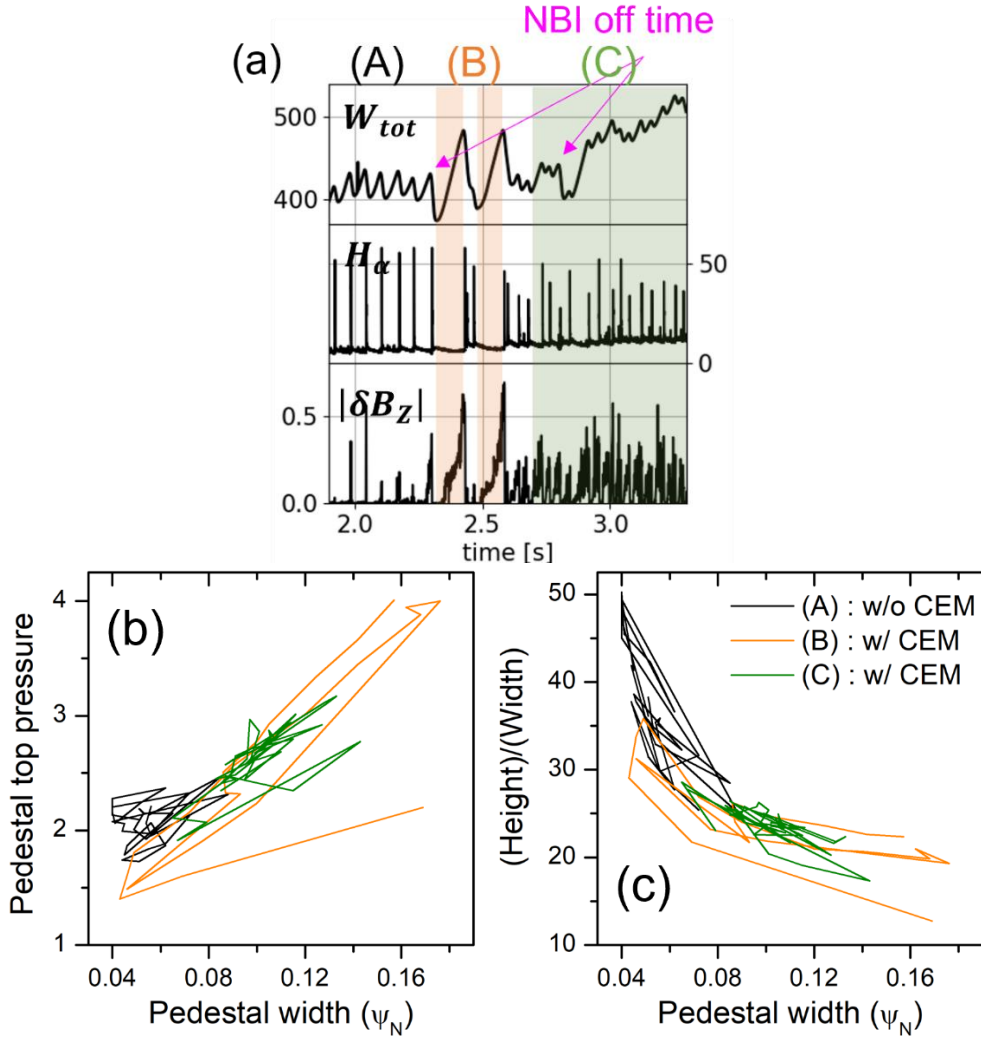
4.1. Changes in pedestal structure

Figure 4.1. (a) Total stored energy measured by the diamagnetic loop (W_{tot}) in kJ, H_α line intensity, and magnetic fluctuation amplitude for CEM ($|\delta B_z|$) in 28030. (A), (B) and (C) on the top of the figure indicate three phases, "without CEM," "Transient high performance with CEM," and "Permanent high performance with CEM." (b) and (c) Pedestal width in the normalized poloidal flux grid (ψ_N), pedestal top pressure, and the ratio of pedestal height to width evaluated for several inter−ELM crash periods of each phase.

As shown in section 2.2, the edge confinement improves due to high as well as wide pedestal formation. Figure 4.1(a) shows stored

energy, H_α line intensity, and CEM amplitude measured by Mirnov coil in 28030, another hybrid scenario target discharge. Compared to (A), the low performance phase without CEM, phases (B) and (C) have transient and permanent high performance with CEM activities, respectively. In figures 4.1(b) and (c), the evolution of the pedestal width, pedestal top pressure, and the pedestal height to width ratio are shown for almost all inter-ELM crash periods in (A), (B), and (C). To evaluate the pedestal parameters, $T_e = T_i$ is assumed, the pedestal width is fixed as that of T_i, and the pedestal top electron density is determined by the line average density measured for the outer region. In (A), the evolution of pedestal width and top pressure stays in the lower left in figure 4.1(b). On the other hand, in (B), both increase during the inter-ELM crash period up to the upper right in figure 4.1(b). Since the multiplication of pedestal width and top pressure is roughly proportional to the thermal energy stored in the pedestal, higher edge confinement is expected in (B). However, the improved edge confinement in (B) is not sustained and is completely lost after the following consecutive ELM crashes, so it goes back to the lower left in figure 4.1(b). Contrarily, even though smaller than in (B), the width and top pressure in (C) stays in the middle of figure 4.1(b), which means permanently improved edge confinement compared to in (A).

Interestingly, the average pedestal pressure gradient represented as the pedestal height to width ratio shown in figure 4.1(c) tends to decrease for the improved edge confinement in (B) and (C). As already mentioned in section 3.2, since the characteristics of the edge transport determine the pedestal pressure gradient, the lower pedestal pressure gradient in (B) and (C) is consistent with the increased transport during CEM activities. Additionally, it also implies that the edge confinement enhancement with CEM activities is not relevant to the improved ideal PBM stability in which the enhanced maximum pedestal pressure gradient is expected, such as in [42,43]. In short, the edge thermal energy improvement introduced in section 2.2 is attributed to the changes in the pedestal structure, the wider and higher pedestal formation,

which is believed to be related to CEM activities.

4.2. Changes in ELM crash and resulting confinement improvement
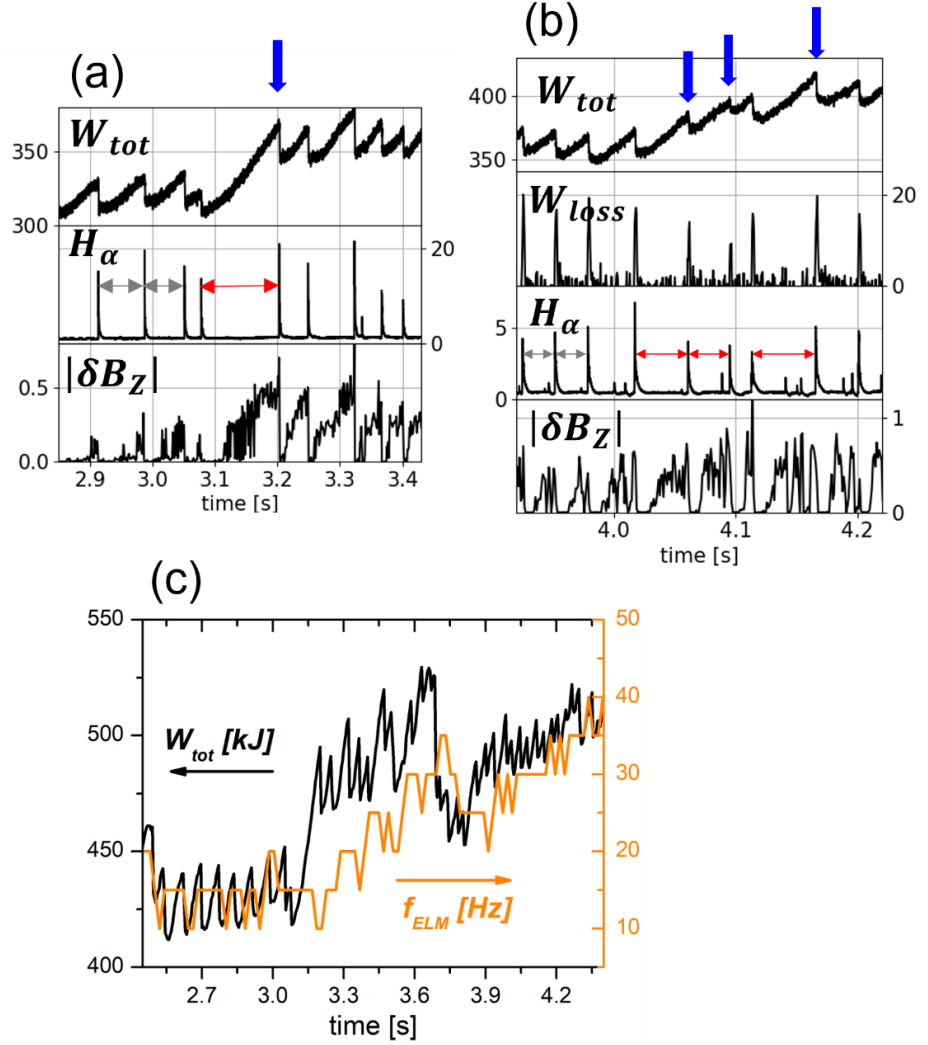
Figure 4.2. (a) and (b) Total stored energy measured by the diamagnetic loop (W_{tot}) in kJ, H_α line intensity, magnetic fluctuation amplitude for CEM ($|\delta B_z|$), and energy loss (W_{loss}) in kJ. (a) and (b) are in 26417 and 25457, respectively. The bidirectional arrows in grey and red represent the length of the inter−ELM crash period in the typical ELM cycles and the CEM dominant cases, respectively. The blue arrows indicate the ELM crashes at which the energy loss

is smaller than the energy recovery during the inter−ELM crash period. (c) Total stored energy (W_{tot}) in kJ and ELM crash frequency (f_{ELM}) in Hz.

Considering the reduced pedestal gradient due to the increased transport with CEM activities, the edge confinement improvement is counterintuitive. Another necessary condition for improving edge confinement with CEM activities is modified ELM crash characteristics. Figure 4.2(a) and (b) show two examples of the performance improvement with a modified ELM crash with CEM activities. In figure 4.2(a), the primary increase of stored energy occurs during the period of $3.08 − 3.2\,s$ with the first strong CEM growth. Compared to the inter−ELM crash periods before $3.08\,s$, the period of 3.08–$3.2\,s$ is a factor of two longer. As shown in the previous section, since pedestal width and height keep increasing until the following ELM crash, the extended inter−ELM period or pedestal recovery phase is responsible for the performance improvement. Additionally, it should be noted that the increased stored energy is not completely lost after the ELM crash, and the improved performance is sustained. It results from smaller energy loss at the ELM crash compared to the increase in the recovery phase, i.e., weakened ELM crash. Figure 4.2(b) shows consecutive performance improvement in the CEM dominant phase due to the extended inter−ELM crash period and weakened ELM crashes. From the ELM cycle after $4.02\,s$, the inter−ELM crash period becomes longer, and the energy loss at the ELM crash is reduced, resulting in the continuous increase of stored energy.

After the performance is improved, stored energy saturates as the ELM crash becomes more frequent. In figure 4.2(c), increased ELM crash frequency in the improved performance phase is shown. Increased ELM crash frequency means a reduced pedestal recovery phase. Hence, the increase of stored energy during the pedestal recovery phase and the decrease at the following ELM crash become balanced, and stored energy saturates.

The reason why the ELM crash characteristics are modified with

CEM activities is still unclear, but the deformation of the pedestal structure, such as pedestal broadening or, thereby, reduced pedestal pressure gradient, might be responsible for it. For example, the weakened ELM crash might be due to the extended width and reduced pressure gradient because the energy lost by the ELM crash is maximized close to the separatrix. Meanwhile, the increased ELM crash frequency after the performance enhancement seems to be due to the weakened ELM crashes. As ELM crashes become weak and the edge energy lost by ELM crashes is reduced, the pedestal pressure gradient in the following ELM cycle begins high, resulting in the earlier ELM crash. Notably, earlier CEM onset during the frequent ELM crash phase, such as after $3.2\,s$ in figure 4.2(a), is consistent with the supposed.
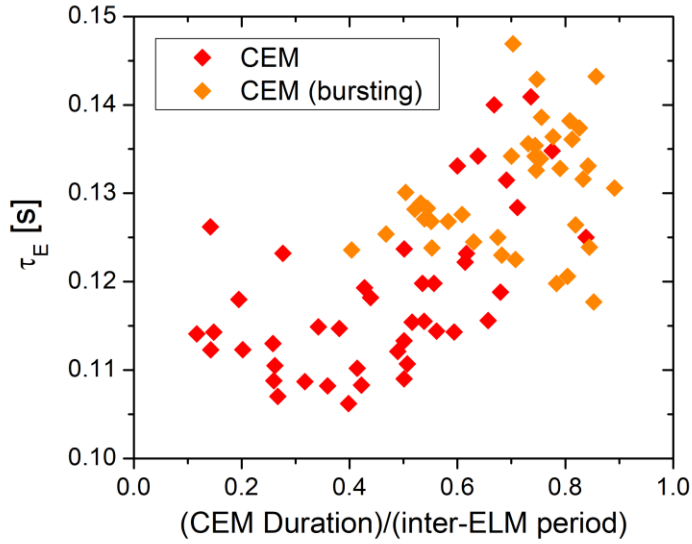
Figure 4.3. The ratio of CEM duration to the inter−ELM crash period vs. global energy confinement time in s. The red and yellow diamonds indicate typical and burst−like CEM, respectively.

The positive correlation between the ratio of CEM duration to inter−ELM crash period and global energy confinement time evaluated right before the ELM crash in figure 4.3 supports the effect of CEM on the edge confinement improvement. The ratio of CEM

duration to inter－ELM crash period parameterizes how long CEM is involved in the pedestal recovery. Because edge thermal energy increases with pedestal broadening under CEM activities, a sufficient CEM lifetime is required to modify the pedestal structure. Therefore, the high value of the ratio of CEM duration to inter－ELM crash period implies that the pedestal is deformed enough to increase edge thermal energy, which is represented by the enhanced global energy confinement time. Additionally, the high value of the ratio of CEM duration to inter－ELM crash period also indicates either an extended pedestal recovery phase with CEM activities during the performance enhancement process or the early CEM onset in the frequent ELM crash phase in the high－performance phase. Both represent high performance. On the other hand, the short－lived CEM, typically of low mode amplitude, does not have enough time to modify the pedestal, resulting in low performance.

Chapter 5. Effect of CEM on the core confinement improvement

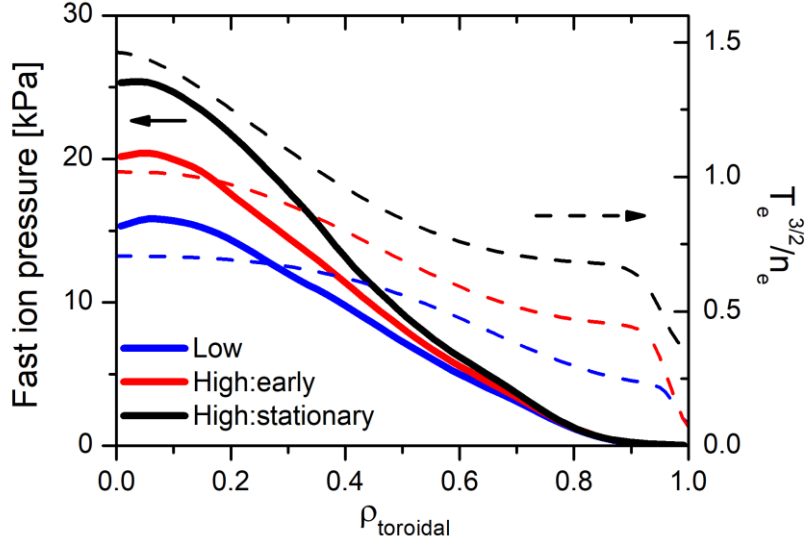## 5.1. Fast ion confinement improvement

Figure 5.1. Fast ion pressure profile in kPa and $T_e^{3/2}/n_e$ for three phases shown in figure 2.2.

Density decrease, one of two primary changes in plasma with CEM activities introduced in section 3.2, directly affects fast ion confinement. In KSTAR, most fast ions originate from the three NBIs: the primary heating and current−driving sources. Hence, in case the same NBI configuration is used, such as in 25452 and 25458 in section 2, the total fast ion energy is determined primarily by beam slowing down time. Since beam slowing down time represents the characteristic time for the thermalization of externally injected beam ions, fast ion content in the core plasma is proportional to beam slowing down time. Due to $T_e^{3/2}/n_e$ dependency of beam slowing down time, density decrease with CEM activities directly increases fast ion content. Figure 5.1 shows that fast ion pressure in three performance phases shown in section 2.2 increases with $T_e^{3/2}/n_e$, which verifies the effect of density decrease on the fast ion energy enhancement.

5.2. Core thermal confinement improvement

In the absence of the MHD modes degrading plasma confinement,

such as NTM or Alfven eigenmode, improvement in the core thermal energy is expected due to the weakened microturbulence activities. The core thermal energy improvement between 'High: early' and 'High: stationary' shown in section 2.2 is the case. Only $m/n = 1/1$ internal kink-like mode, where m and n are poloidal and toroidal mode numbers, exists inside $\rho_{toroidal} = 0.1$ in 'High: early' and is stabilized in 'High: stationary', which is not relevant to the thermal pressure enhancement for $\rho_{toroidal} < 0.5$ between 'High: early' and 'High: stationary.'

To analyze the core thermal energy confinement improvement between 'High: early' and 'High: stationary,' linear analysis of microturbulence is conducted at $\rho_{toroidal} \cong 0.4$ by GKW code. For GKW inputs, kinetic electron and electromagnetic effect are considered, and realistic equilibrium reconstructed by kinetic-EFIT is used. In addition, fast ions calculated by NUBEAM code are included by assuming it as an additional deuterium species with significantly high temperature and low density. All rotational effect, including parallel flow shear or $E \times B$ flow shear, is not considered. This assumption is verified by the fact that the toroidal rotation gradient, which plays a dominant role in determining the parallel flow shear or $E \times B$ flow shear in the core region in KSTAR, is almost similar in both phases, as shown in figure 2.2.
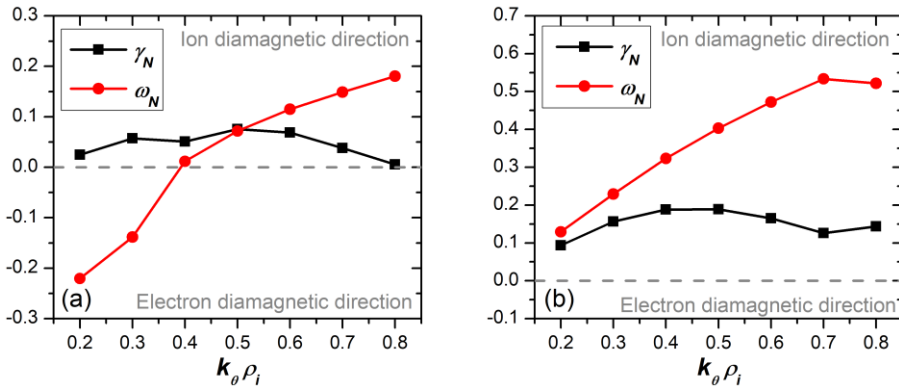

Figure 5.2. Wavenumber, $k_\theta \rho_i$, scans for linear growth rate, γ_N, and real frequency, ω_N, normalized by $R/V_{th,i}$ at $\rho_{toroidal} \cong 0.4$ in (a) "High: early" and "High: stationary" defined in figure 2, respectively. k_θ, ρ_i, R, and $V_{th,i}$ are wavenumber in the poloidal

direction, ion gyro−radius, major radius, and ion thermal speed, respectively. Positive and negative ω_N indicate ion and electron diamagnetic directions.

Figure 5.2(a) and (b) show wavenumber scans at $\rho_{toroidal} \cong 0.4$ in 'High: early' and 'High: stationary', respectively. In both phases, the maximum linear growth rate is found at $k_\theta \rho_i = 0.5$, where k_θ and ρ_i are wavenumber in the poloidal direction and ion gyro−radius, and both most unstable modes propagate in the ion diamagnetic direction. Therefore, in both 'High' phases, ITG mode is believed to dominate the heat transport in the inner core region. It is consistent with the previous study on the high−performance hybrid scenario discharges in KSTAR [43].
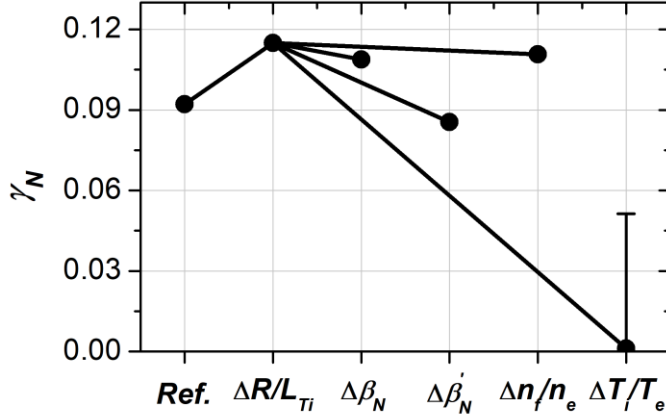

Figure 5.3. Normalized linear growth rate, γ_N, calculated for $k_\theta \rho_i = 0.5$ at $\rho_{toroidal} \cong 0.4$ in "High: early" and "High: stationary" introduced in figure 2. *Ref.* indicates "High: early". $\Delta R/L_{Ti}$ is the case that only R/L_{Ti} is increased to the value in "High: stationary". $\Delta \beta_N$, $\Delta \beta'_N$, $\Delta n_f/n_e$, and $\Delta T_i/T_e$ indicate the cases that β_N, β'_N, n_f/n_e, and T_i/T_e are additionally changed to that in "High: stationary", respectively. The error bar of $\Delta T_i/T_e$ is evaluated for 10 % increased T_e considering the uncertainty in T_e measurement.

To compare relative stabilization effect quantitatively, figure 5.3 represents the linear growth rate of the mode with $k_\theta \rho_i = 0.5$ for various cases. '*Ref.*' indicates 'High: early' case. '$\Delta R/L_{Ti}$' is the case that R/L_{Ti}, the free energy source of ITG mode, is replaced by the

value in 'High: stationary' to analyze the effect of increased R/L_{Ti} on ITG mode. R and L_{Ti} is a major radius and an ion temperature gradient length defined as $L_{Ti} \equiv T_i/\nabla T_i$, respectively. It shows that the linear growth rate is increased compared to '$Ref.$', which verifies that the mode is ITG mode. The other four cases, '$\Delta \beta_N$', '$\Delta \beta_N'$', '$\Delta n_f/n_e$', and '$\Delta T_i/T_e$', indicate the cases that one more parameter is replaced by that of 'High: stationary' to evaluate the effect of ITG mode stabilization by the change in each parameter. The increase in β_N', the normalized equilibrium pressure gradient, and T_i/T_e shows a considerable decrease in the linear growth rate compared to '$Ref.$' as well as '$\Delta R/L_{Ti}$'. It implies that ITG mode activities are reduced compared to 'High: early' even in the increased R/L_{Ti}. On the other hand, for the increase in β_N and n_f/n_e, the normalized equilibrium pressure and fast ion fraction, respectively, the stabilization effect exists but is relatively small. Especially, the n_f/n_e effect, representing thermal ion dilution, is little, probably due to the small fraction of fast ions of less than 5% electron density.

Since there are no externally applied actuators such as electron cyclotron resonance heating between 'High: early' and 'High: stationary', the increase of β_N' and T_i/T_e seems to be attributed to density decrease. As discussed in section 5.1, density decrease enhances fast ion pressure, and the increase of centrally peaked fast ion pressure contributes to β_N'. Indeed, the electromagnetic stabilization of ITG mode provided by the fast ion pressure gradient is known to be effective linearly and non-linearly [44,45]. Additionally, density decrease could decouple ion and electron temperature by reducing collisional equilibration of ion and electron thermal energy. It allows T_i/T_e to increase in the case of dominant ion heating as in KSTAR, where three NBIs provide power to ions by 40% more than to electrons. Moreover, once β_N' or T_i/T_e is increased, the positive feedback loop of ITG stabilization [17-19,46,47] could be expected; the increase of β_N' and T_i/T_e stabilizes ITG mode, thereby R/L_{Ti} increases, which improves β_N' and T_i/T_e.
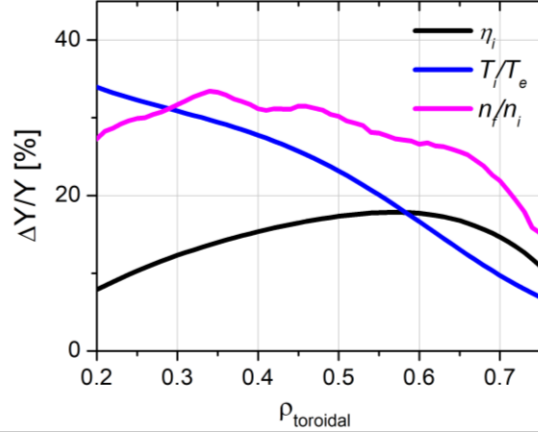
Figure 5.4. % changes, $\Delta Y/Y$, in $\eta_i \equiv d\ln T_i/d\ln n_i$, T_i/T_e, and n_f/n_i from "High: early" to "High: stationary" defined in figure 2.2.

Figure 5.4 shows the % change of η_i, T_i/T_e, and n_f/n_i in the core region between 'High: early' and 'High: stationary', where n_i is thermal ion density. η_i determined by ITG mode activities increases with T_i/T_e, and n_f/n_i, representing weakened ITG mode activities at the enhanced T_i/T_e, and n_f/n_i. Even though the quantitative comparison for the stabilizing effect of T_i/T_e, and n_f/n_i is not available, the increase of η_i at the elevated T_i/T_e, and n_f/n_i implies that both are contributing to the ITG stabilization, which is consistent with the linear analysis.

Chapter 6. Conclusion

6.1. Summary

This dissertation investigates the origin of performance improvement observed in KSTAR hybrid scenario discharges by analyzing two representative discharges, 25452 with high performance and 25458 with low performance. The performance improvement primarily originates from the enhanced edge confinement due to wide and high pedestal formation. In addition, the increase in fast ion energy accounts for a third of the improved performance. Even though the

net change of the core thermal energy is negative due to reduced core volume resulting from the expansion of the edge volume, the enhanced thermal energy in the inner core region, $\rho_{toroidal} < 0.5$, limits the degradation.

Coherent edge mode (CEM) is suggested as a trigger and sustainment mechanism for the high performance. CEM is a coherent electromagnetic mode and is localized in the edge region. CEM is triggered in the middle of the pedestal recovery phase and tends to increase particle and heat transport in the edge region. Observed with CEM activities, a pedestal broadening and a density decrease, two primary changes in plasma, are believed to be responsible for the edge and core confinement improvement, respectively.
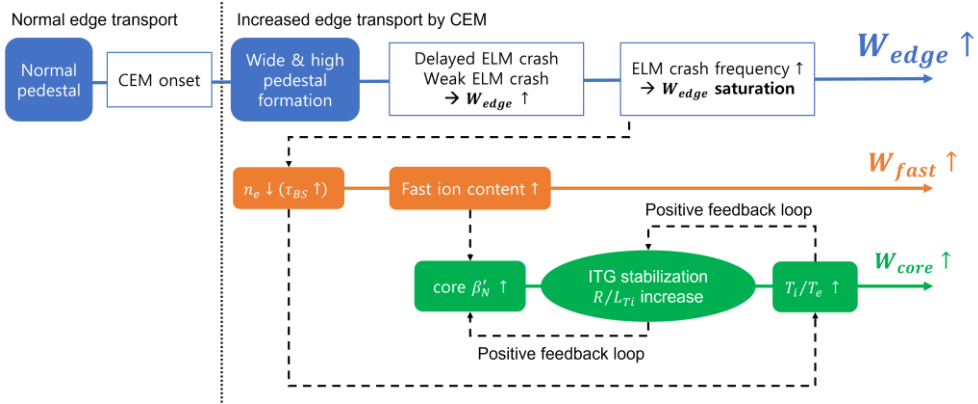

Figure 6.1. Flow chart for the performance improvement with CEM activities. W_{edge}, W_{fast}, and W_{core} are edge thermal, fast ion, and core thermal energy, respectively. τ_{BS} is beam slowing down time.

Figure 6.1 represents the flow chart to describe the performance improvement observed with CEM activities. After CEM is triggered, the edge transport is increased, and a wide and high pedestal is formed. Then, the edge thermal energy is increased by delayed and weakened ELM crashes and, finally, saturates due to the increased ELM crash frequency in the high−performance phase. Meanwhile, plasma density decreases in the CEM dominant phase. Due to the extended beam slowing down time, fast ion content, i.e., fast ion energy, is increased. In addition, the decrease of density and the increase of fast ion content contribute to T_i/T_e and β'_N, respectively, improving the stability of ITG mode, the dominant microturbulence in

the core region. Stabilization of ITG mode increases R/L_{Ti}, which enhances T_i/T_e and β_N'. In other words, ITG mode stabilization is reinforced by positive feedback loops of T_i/T_e and β_N'. Consequently, core thermal energy is enhanced.

6.2. Concluding remarks and future works

This dissertation is meaningful in that, for the first time, it studied the CEM effects on the performance of KSTAR hybrid scenarios. It suggests that researchers should check CEM activities in KSTAR hybrid scenario experiments for high performance. For example, suppose high performance is not reproduced in hybrid scenario experiments. In that case, the absence of CEM activities could be the reason. In addition, this study provides an explanation for core and edge confinement improvement attributable to CEM activities, which helps researchers to understand experimentally observed changes in core and edge plasma with CEM activities and to distinguish the phenomena related to CEM activities from others.

Nevertheless, there remain unsolved subjects. First, the onset condition of CEM should be investigated. Finding the robust onset condition of CEM would provide more controllability in developing high−performance hybrid scenarios. The preliminary analysis found that CEM is excited in relatively high−density plasma provided by external fueling or wall retention. In addition, assuming that CEM onset follows the ideal PBM stability, it showed that CEM onset at a relatively high density is due to the weakened ion diamagnetic stabilization effect. Still, some exceptional cases exist, such that, for two discharges at the same density, one has CEM, and the other does not have CEM. Secondly, optimization of CEM activities is necessary for more improved core confinement. As shown in sections 2 and 3, CEM has a finite amplitude in the outer core region, so the stiffness of thermal pressure is broken there, which degrades core thermal confinement. Therefore, if CEM activities could be more localized 'in' the pedestal region, the core thermal energy would be more enhanced. Thirdly, decreased toroidal rotation shear effect on pedestal

structure, i.e., pedestal confinement, needs to be investigated. As shown in section 2, toroidal rotation shear is significantly reduced in the edge region during the high-performance transition. Since the edge toroidal rotation shear is known to play a considerable role in forming a pedestal structure by reducing transport in the pedestal through $E \times B$ shearing, the independent effect of the decreased toroidal rotation shear should be investigated. Additionally, the effects of increased toroidal rotation shear in the core, due to the edge toroidal rotation decrease, on the core thermal confinement should be studied. Finally, heat flux on plasma-facing components (PFCs) in the CEM dominant phase needs to be checked. For the fusion reactor operation, heat flux on PFCs must be low enough for PFCs to sustain long fusion plasma operations. Since CEM tends to increase particle and heat transport during the inter-ELM crash period and weaken ELM crash, heat flux to PFCs is expected to vary.

Bibliography

[1]   Sips A C C 2005 Advanced scenarios for ITER operation *Plasma Physics and Controlled Fusion* vol 47

[2]   Gormezano C, Sips A C C, Luce T C, Ide S, Becoulet A, Litaudon X, Isayama A, Hobirk J, Wade M R, Oikawa T, Prater R, Zvonkov A, Lloyd B, Suzuki T, Barbato E, Bonoli P, Phillips C K, Vdovin V, Joffrin E, Casper T, Ferron J, Mazon D, Moreau D, Bundy R, Kessel C, Fukuyama A, Hayashi N, Imbeaux F, Murakami M, Polevoi A R and st. John H E 2007 Chapter 6: Steady state operation *Nuclear Fusion* **47**

[3]   Luce T C, Challis C D, Ide S, Joffrin E, Kamada Y, Politzer P A, Schweinzer J, Sips A C C, Stober J, Giruzzi G, Kessel C E, Murakami M, Na Y S, Park J M, Polevoi A R, Budny R v., Citrin J, Garcia J, Hayashi N, Hobirk J, Hudson B F, Imbeaux F, Isayama A, McDonald D C, Nakano T, Oyama N, Parail V v., Petrie T W, Petty C C, Suzuki T and Wade M R 2014 Development of advanced inductive scenarios for ITER *Nuclear Fusion* **54**

[4]   Zohm H, Gantenbein G, Isayama A, Keller A, Haye L, Maraschek M, Mück A, Nagasaki K, Pinches S D and Strait E J 2003 *Plasma Phys. Control. Fusion 45 A163 Plasma Phys* vol 45

[5]   Citrin J, Jenko F, Mantica P, Told D, Bourdelle C, Garcia J, Haverkort J W, Hogeweij G M D, Johnson T and Pueschel M J 2013 Nonlinear stabilization of tokamak microturbulence by fast ions *Physical Review Letters* **111**

[6]   Hahm T S and Tang W M 1989 Properties of ion temperature gradient drift instabilities in H−mode plasmas *Physics of Fluids B* **1** 1185−92

[7]   Burrell K H, Carlstrom T N, Doyle E J, Finkenthal D, Gohil：P, Groebner R J, Hillis D L, Kim J, Matsumoto H, Moyer，' R A, Osborne T H, Rettig C L, Peebles W A, Rhodes T L, Stjohn ' H, Stambaugh R D, Wade M R and Watkins' J G *PHYSICS OF THE 1−MODE TO H−MODE TRANSITION IN TOKAMAKS* vol 34

[8]   Zohm H 1996 *Plasma Physics and Controlled Fusion Edge localized modes (ELMs) Edge localized modes (ELMs)* vol 38

[9]   Leonard A W 2014 Edge−localized−modes in tokamaks *Physics of Plasmas* **21**

[10]   Shimada M, Campbell D J, Mukhovatov V, Fujiwara M, Kirneva N, Lackner K, Nagami M, Pustovitov V D, Uckan N, Wesley J, Asakura N, Costley A E, Donné A J H, Doyle E J, Fasoli A, Gormezano C, Gribov Y, Gruber O, Hender T C, Houlberg W, Ide S, Kamada Y, Leonard A, Lipschultz B, Loarte A, Miyamoto K, Mukhovatov V, Osborne T H, Polevoi A and Sips A C C 2007 Chapter 1: Overview and summary *Nuclear Fusion* **47**

[11]   Citrin J, Hobirk J, Schneider M, Artaud J F, Bourdelle C, Crombe K, Hogeweij G M D, Imbeaux F, Joffrin E, Koechl F and Stober J 2012 Predictive analysis of q−profile influence on transport in JET and

ASDEX Upgrade hybrid scenarios *Plasma Physics and Controlled Fusion* **54**

[12]   Voitsekhovitch I, Belo P, Citrin J, Fable E, Ferreira J, Garcia J, Garzotti L, Hobirk J, Hogeweij G M D, Joffrin E, Köchl F, Litaudon X, Moradi S and Nabais F 2014 Modelling of JET hybrid scenarios with GLF23 transport model: E ×b shear stabilization of anomalous transport *Nuclear Fusion* **54**

[13]   Citrin J, Garcia J, Görler T, Jenko F, Mantica P, Told D, Bourdelle C, Hatch D R, Hogeweij G M D, Johnson T, Pueschel M J and Schneider M 2015 Electromagnetic stabilization of tokamak microturbulence in a high−β regime *Plasma Physics and Controlled Fusion* **57**

[14]   Maggi C F, Groebner R J, Oyama N, Sartori R, Horton L D, Sips A C C, Suttrop W, Leonard A, Luce T C, Wade M R, Kamada Y, Urano H, Andrew Y, Giroud C, Joffrin E and de La Luna E 2007 Characteristics of the H−mode pedestal in improved confinement scenarios in ASDEX upgrade, DIII−D, JET and JT−60U *Nuclear Fusion* vol 47 pp 535−51

[15]   Na Y S, Lee Y H, Byun C S, Kim S K, Lee C Y, Park M S, Yang S M, Kim B, Jeon Y M, Choi G J, Citrin J, Juhn J W, Kang J S, Kim H S, Kim J H, Ko W H, Kwon J M, Lee W C, Woo M H, Yi S, Yoon S W and Yun G S 2020 On hybrid scenarios in KSTAR *Nuclear Fusion* **60**

[16]   Yushmanov P N, Takizuka T, Riedel K S, Kardaun O J W F, Cordey J G, Kaye S M and Post D E 1990 Scalings for tokamak energy confinement *Nuclear Fusion* **30** 1999

[17]   Weiland J, Asp E, Garbet X, Mantica P, Parail V, Thomas P, Suttrop W and Tala T 2005 Effects of temperature ratio on JET transport in hot ion and hot electron regimes *Plasma Physics and Controlled Fusion* **47** 441−9

[18]   Asp E, Weiland J, Garbet X, Mantica P, Parail V and Suttrop W 2005 JETTO simulations of Te/Ti effects on plasma confinement *Plasma Physics and Controlled Fusion* **47** 505−19

[19]   Kim H T, Sips A C C, Romanelli M, Challis C D, Rimini F, Garzotti L, Lerche E, Buchanan J, Yuan X, Kaye S, Litaudon X, Abduallev S, Abhangi M, Abreu P, Afzal M, Aggarwal K M, Ahlgren T, Ahn J H, Aho−Mantila L, Aiba N, Airila M, Albanese R, Aldred V, Alegre D, Alessi E, Aleynikov P, Alfier A, Alkseev A, Allinson M, Alper B, Alves E, Ambrosino G, Ambrosino R, Amicucci L, Amosov V, Sundén E A, Angelone M, Anghel M, Angioni C, Appel L, Appelbee C, Arena P, Ariola M, Arnichand H, Arshad S, Ash A, Ashikawa N, Aslanyan V, Asunta O, Auriemma F, Austin Y, Avotina L, Axton M D, Ayres C, Bacharis M, Baciero A, Baião D, Bailey S, Baker A, Balboa I, Balden M, Balshaw N, Bament R, Banks J W, Baranov Y F, Barnard M A, Barnes D, Barnes M, Barnsley R, Wiechec A B, Orte L B, Baruzzo M, Basiuk V, Bassan M, Bastow R, Batista A, Batistoni P, Baughan R, Bauvir B, Baylor L, Bazylev B, Beal J, Beaumont P S, Beckers M, Beckett B, Becoulet A, Bekris N, Beldishevski M, Bell K, Belli F, Bellinger M, Belonohy, Ayed N ben, Benterman N A, Bergsåker H, Bernardo J, Bernert M, Berry M, et al 2018 High fusion performance at high Ti/Te in JET−ILW baseline plasmas with high NBI heating

power and low gas puffing *Nuclear Fusion* **58**

[20]   Peeters A G, Camenen Y, Casson F J, Hornsby W A, Snodin A P, Strintzi D and Szepesi G 2009 The nonlinear gyro−kinetic flux tube code GKW *Computer Physics Communications* **180** 2650–72

[21]   Ko S H, Kwon J M, Ko W H, Kim S S, Jhang H and Terzolo L 2016 Characteristics of toroidal rotation and ion temperature pedestals between ELM bursts in KSTAR H−mode plasmas *Physics of Plasmas* **23**

[22]   Snyder P B, Wilson H R, Osborne T H and Leonard A W 2004 Characterization of peeling−ballooning stability limits on the pedestal *Plasma Physics and Controlled Fusion* vol 46 (Institute of Physics Publishing)

[23]   Lee J H, Oh S, Wi H M, Lee W R, Kim K P, Yamada I, Narihara K and Kawahata K 2012 Tangential Thomson scattering diagnostic for the KSTAR tokamak *Journal of Instrumentation* **7**

[24]   Ko W H, Lee H, Seo D and Kwon M 2010 Charge exchange spectroscopy system calibration for ion temperature measurement in KSTAR *Review of Scientific Instruments* vol 81

[25]   Juhn J W, Lee K C, Lee T G, Wi H M, Kim Y S, Hahn S H and Nam Y U 2021 Multi−chord IR−visible two−color interferometer on KSTAR *Review of Scientific Instruments* **92**

[26]   Lao L, Ferron J, Groebner R, Howl W, St JOHN H, Strait E and Taylor T 1990 Equilibrium analysis of current profiles in tokamaks *Nuclear Fusion* **30** 1035

[27]   Ltitjens H, Bondeson A and Sauter O 1996 *The CHEASE code for toroidal MHD equilibria* vol 97

[28]   Pankin A, McCune D, Andre R, Bateman G and Kritz A 2004 The tokamak Monte Carlo fast ion module NUBEAM in the national transport code collaboration library *Computer Physics Communications* **159** 157–84

[29]   Liberman 4s, Pinard J and Crance ; M 1976 *PHYSICAL REVIEW LETTERS Study of High−Beta Magnetohydrodynamic Modes and Fast−Ion Losses in PDX* vol 50

[30]   Wong K L, Fonck R J, Paul S F, Roberts, ' D R, Fredrickson E D, Nazikian R, Park H K, Bell M, Bretz N L, Budny R, Cohen S, Hammett G W, Jobes F C, Meade D M, Medley S S, Mueller D, Nagayama Y, Owens D K and Synakowski E J 1991 *Excitation of Toroidal Alfven Eigenmodes in TFTR* vol 66

[31]   Nam Y U, Zoletnik S, Lampert M and Kovácsik A 2012 Analysis of edge density fluctuation measured by trial KSTAR beam emission spectroscopy system *Review of Scientific Instruments* vol 83

[32]   Yun G S, Lee W, Choi M J, Kim J B, Park H K, Domier C W, Tobias B, Liang T, Kong X, Luhmann N C and Donń A J H 2010 Development of KSTAR ECE imaging system for measurement of temperature fluctuations and edge density fluctuations *Review of Scientific Instruments* vol 81

[33]   Tang W M, Connor J W and Hastie R J 1980 Kinetic−ballooning−mode theory in general geometry *Nuclear Fusion* **20** 1439

[34]   Perez C P, Koslowski H R, Huysmans G T A, Hender T C, Smeulders P, Alper B, de La Luna E, Hastie R J, Meneses L, Nave M F F, Parail V and Zerbini M 2004 Type-I ELM precursor modes in JET *Nuclear Fusion* **44** 609-23

[35]   Snyder P B, Wilson H R and Xu X Q 2005 Progress in the peeling-ballooning model of edge localized modes: Numerical studies of nonlinear dynamics *Physics of Plasmas* vol 12 pp 1-7

[36]   Huysmans G T A and Czarny O 2007 MHD stability in X-point geometry: Simulation of ELMs *Nuclear Fusion* vol 47 pp 659-66

[37]   Yun G S, Lee W, Choi M J, Lee J, Park H K, Tobias B, Domier C W, Luhmann N C, Donné A J H and Lee J H 2011 Two-dimensional visualization of growth and burst of the edge-localized filaments in KSTAR H-mode plasmas *Physical Review Letters* **107**

[38]   Kirk A, Dunai D, Dunne M, Huijsmans G, Pamela S, Becoulet M, Harrison J R, Hillesheim J, Roach C and Saarelma S 2014 Recent progress in understanding the processes underlying the triggering of and energy loss associated with type i ELMs *Nuclear Fusion* **54**

[39]   Kim M, Park H K, Lee J, Yun G S, Xu X Q and Bécoulet M 2019 BOUT++ nonlinear simulation for a comparative study with the measured 2D ELM structures in the KSTAR H-mode plasma *Physics of Plasmas* **26**

[40]   Perez Von Thun C, Frassinetti L, Horvath L, Saarelma S, Meneses L, de La Luna E, Beurskens M, Boom J, Flanagan J, Hillesheim J C, Maggi C F, Pamela S J P and Solano E R 2019 Long-lived coupled peeling ballooning modes preceding ELMs on JET *Nuclear Fusion* **59**

[41]   Snyder P B, Groebner R J, Hughes J W, Osborne T H, Beurskens M, Leonard A W, Wilson H R and Xu X Q 2011 A first-principles predictive model of the pedestal height and width: Development, testing and ITER optimization with the EPED model *Nuclear Fusion* **51**

[42]   Maggi C F, Groebner R J, Oyama N, Sartori R, Horton L D, Sips A C C, Suttrop W, Leonard A, Luce T C, Wade M R, Kamada Y, Urano H, Andrew Y, Giroud C, Joffrin E and de La Luna E 2007 Characteristics of the H-mode pedestal in improved confinement scenarios in ASDEX upgrade, DIII-D, JET and JT-60U *Nuclear Fusion* vol 47 pp 535-51

[43]   Na Y S, Lee Y H, Byun C S, Kim S K, Lee C Y, Park M S, Yang S M, Kim B, Jeon Y M, Choi G J, Citrin J, Juhn J W, Kang J S, Kim H S, Kim J H, Ko W H, Kwon J M, Lee W C, Woo M H, Yi S, Yoon S W and Yun G S 2020 On hybrid scenarios in KSTAR *Nuclear Fusion* **60**

[44]   Citrin J, Jenko F, Mantica P, Told D, Bourdelle C, Garcia J, Haverkort J W, Hogeweij G M D, Johnson T and Pueschel M J 2013 Nonlinear stabilization of tokamak microturbulence by fast ions *Physical Review Letters* **111**

[45]   Citrin J, Garcia J, Görler T, Jenko F, Mantica P, Told D, Bourdelle C, Hatch D R, Hogeweij G M D, Johnson T, Pueschel M J and Schneider M 2015 Electromagnetic stabilization of tokamak microturbulence in a high-β regime *Plasma Physics and Controlled Fusion* **57**

[46]   Bourdelle C, Dorland W, Garbet X, Hammett G W, Kotschenreuther

M, Rewoldt G and Synakowski E J 2003 Stabilizing impact of high gradient of β on microturbulence *Physics of Plasmas* **10** 2881–7

[47] Bourdelle C, Hoang G T, Litaudon X, Roach C M and Tala T 2005 Impact of the a parameter on the microstability of internal transport barriers *Nuclear Fusion* **45** 110–30

초록

미래에 성공적인 핵융합발전소 운전을 위해서는 높은 성능의 장시간 운전이 필수적이다. 핵융합 플라즈마는 복잡한 시스템이고 자가 충족적으로 변하기 때문에, 고성능 천이와 유지의 메커니즘을 이해하는 것이 중요하다. 국내 핵융합 실험 장치 KSTAR(Kstar Superconducting Tokamak Advanced Research)에서는 국제 핵융합 실험로 ITER(International Thermonuclear Experimental Reactor)의 후보 운전시나리오 중 하나인 하이브리드 시나리오의 고성능 메커니즘에 대한 연구가 수년간 수행되어 왔다. 이 학위 논문에서는 KSTAR 하이브리드 시나리오의 고성능 천이와 유지의 주요한 원인으로 가장자리 코히어런트 모드(CEM)를 제안한다.

CEM은 코히어런트 전자기 모드로서 가장자리 영역에 존재한다. CEM은 Edge localized mode (ELM) 붕괴 사이클 중 받침대 구조(pedestal) 회복 단계에서 발생하고 ELM 붕괴 이후 안정화된다. CEM은 가장자리의 입자 및 열 수송을 증가시키며, 이로 인해 넓은 pedestal이 형성되고 플라즈마 밀도가 감소한다. 흥미롭게도, 가장자리의 증가된 수송에 의해 일어난 이 두 가지 결과는 각각 가장자리와 중심부 가둠 성능 향상에 기여한다.

넓어진 pedestal에서는 ELM 붕괴가 지연되고 약해진다. 다시 말하면, 연장된 pedestal 회복 단계에 의해 pedestal의 높이가 높아지고, ELM 붕괴로 인한 에너지 손실이 작아진다. 결과적으로, 넓고 높아진 pedestal에 더 많은 에너지가 저장될 수 있다.

또 다른 결과인 플라즈마 밀도의 감소는 고속 이온 가둠 성능에 직접적으로, 중심부 열 가둠 성능에는 간접적으로 기여한다. 낮춰진 플라즈마 밀도에서는, 고속 이온의 열운동화가 지연되어 고속 이온이 더 오랫동안 플라즈마 중심부에 머무른다. 다시 말해, 고속 이온의 수가 많아져서, 고속이온에너지가 증가한다.

한편, 중심부의 열 가둠은 중심부 열 가둠을 제약하는 주요한 마이크로터뷸런스인 ion temperature gradient (ITG) 모드의 안정화가 강화되어 향상된다. 자이로키네틱(gyrokinetic) 코드인 GKW를 활용한 마이크로터뷸런스의 선형 해석을 통해 두 가지 지배적인 효과가 밝혀졌다. 하나는 전자기 효과이고, 다른 하나는 이온 전자 온도비다. 전자는 향상된 고속이온 가둠에 의해 강화되고, 후자는 감소한 전자-이온 사이의 감소된 충돌에 의해 증가한다.